crystals

MDPI

Article

Processing Route Dependence of Microstructure and Mechanical Properties in an Al-Li-Mg Alloy for Lightweight Sports Equipment

Ge Liu [1], Shenchen Zhang [2], Yuncheng Zhu [3], Xin Li [2], Yingchao Zhao [2], Dengfeng Yin [2] and Ming-Chun Zhao [2,*]

[1] College of Physical Ehysical Education, Jimei University, Xiamen 361021, China; 199261000026@jmu.edu.cn
[2] School of Materials Science and Engineering, Central South University, Changsha 410083, China; 233112099@csu.edu.cn (S.Z.); 243101040@csu.edu.cn (X.L.); zhaoyc@usc.edu.cn (Y.Z.); 206191@csu.edu.cn (D.Y.)
[3] Department of P.E., Central South University, Changsha 410083, China; 8204221524@csu.edu.cn
* Correspondence: mczhao@csu.edu.cn

Abstract

The pursuit of lightweight, high-performance sports equipment drives the development of Al-Li-Mg alloys, yet systematic studies linking a complete processing route, from as-cast to peak-aged condition, to microstructural evolution and mechanical properties remain limited. This work provides the first comprehensive investigation of how a sequential processing route (homogenization, hot rolling, solution treatment, and peak aging) transforms the coarse as-cast structure of an Al-Li-Mg alloy into a refined, recrystallized grain architecture with a uniform dispersion of nanoscale δ'-Al_3Li precipitates. This microstructural transformation leads to a dramatic enhancement in mechanical properties: the peak-aged alloy exhibits increases of approximately 92%, 139%, and 925% in yield strength, ultimate tensile strength, and elongation, respectively, relative to the as-cast condition. The dominant strengthening mechanism is identified as dislocation shearing of coherent δ'-Al_3Li precipitates (average radius ~5 nm, well below the ~25 nm transition threshold for Orowan looping), which enhances strength without compromising ductility, demonstrating the critical role of the processing route in tailoring microstructures and mechanical properties for lightweight sports equipment.

Keywords: Al-Li-Mg alloys; microstructures; mechanical properties; processing route; lightweight materials; sports equipment

1. Introduction

The pursuit of enhanced athletic performance has continuously driven innovation in sports equipment design and manufacturing, with materials playing a significant role in this evolution. A fundamental and relentless objective is the achievement of weight reduction without compromising structural integrity, durability, or safety. Reducing the mass of equipment such as bicycle frames, tennis rackets, golf club heads, baseball bats, and mountaineering gear directly translates to improved athlete agility, reduced fatigue, and potentially superior kinematic results. The selection and development of materials that offer an optimal synergy of low density, high specific strength (strength-to-weight ratio), and adequate ductility are of critical importance. To date, Al alloys have been established as frontrunners for numerous sporting applications [1–3], owing to their favorable combination of relatively low density, good corrosion resistance, excellent formability, and cost-effectiveness. However, the continuous demand for higher performance standards

Check for updates

Academic Editor: Ferdinando Costantino

Received: 2 April 2026
Revised: 29 April 2026
Accepted: 15 May 2026
Published: 18 May 2026

Copyright: © 2026 by the authors. Licensee MDPI, Basel, Switzerland. This article is an open access article distributed under the terms and conditions of the Creative Commons Attribution (CC BY) license.

necessitates the advancement and optimization of Al alloys with property profiles that exceed those of conventional series.

Al-Li alloys represent a significant advancement in this pursuit through the addition of Li, the lightest metallic element, which confers a substantial reduction in density. The replacement of conventional commercial Al alloys with Al-Li alloys can achieve weight reductions of 10–20% and stiffness increases of 15–20% in structural components [4,5]. This intrinsic characteristic makes Al-Li alloys exceptionally attractive for weight-critical applications. Beyond density reduction, Li contributes to precipitation strengthening through the formation of coherent, ordered δ'-Al_3Li precipitates, which are highly effective in impeding dislocation motion [6]. When combined with Mg, another lightweight element that provides solid solution strengthening and forms additional strengthening phases, the Al-Li-Mg ternary system exhibits considerable potential for developing alloys with an optimal balance of specific strength and stiffness [7,8]. In recent years, extensive studies have been conducted to better understand the microstructure–property relationship in Al-Li-Mg alloys. For instance, Shi et al. [5] investigated the effect of Mg content on the microstructures and mechanical properties of ultralight cast Al-3Li-XMg-0.1Zr alloys, revealing that increasing Mg promotes solid solution strengthening and refines the grain structure. Yin et al. [7] elucidated the role of multi-microalloying (Sc, Zr, Er, Ti) in an Al-Li-Mg alloy, showing that core–shell precipitates contribute to both thermal stability and precipitation strengthening. Mogucheva et al. [8] further demonstrated that severe plastic deformation via equal-channel angular pressing (ECAP) can produce an ultrafine-grained structure in an Al-Li-Mg-Sc-Zr alloy, achieving high strength with reasonable ductility. These studies collectively highlight that the performance of Al-Li-Mg alloys is highly sensitive to both composition and processing, further motivating the effect of a complete processing route tailored for sports equipment applications.

Nevertheless, the advantageous properties of Al-Li-Mg alloys are not solely determined by their compositions; they are profoundly influenced by their microstructures, which are determined by the processing route. The evolution from an as-cast ingot to a finished, high-performance component involves a series of interconnected stages, including homogenization, hot working, solution treatment, and aging, each imposing specific modifications on the microstructure. The initial solidification process typically results in a coarse, chemically heterogeneous structure characterized by dendritic segregation, coarse intermetallic compounds (IMCs) at grain boundaries, and potential casting defects. This as-cast microstructure is generally associated with low ductility, making it unsuitable for demanding applications. Therefore, subsequent processing steps are essential to homogenize the chemical distribution, refine the grain structure, control the morphology and distribution of secondary phases, and ultimately, to introduce a controlled dispersion of nano-scale strengthening precipitates.

Homogenization aims to alleviate microsegregation by dissolving non-equilibrium secondary phases into the α-Al matrix. The subsequent hot working stage, such as rolling or forging, introduces severe plastic deformation. This not only shapes the material but also fundamentally alters its microstructure by elongating grains, fragmenting coarse brittle phases, and storing deformation energy within the lattice [9,10]. The dynamic restoration mechanisms operative during hot working, recovery versus recrystallization, significantly influence the deformation texture and the stored energy available for subsequent static recrystallization [11–13]. Following deformation, solution treatment is typically applied to achieve complete recrystallization, resulting in a fine, equiaxed grain structure, and to take alloying elements into solid solution. The final aging treatment then precipitates the strengthening phases, such as the δ'-Al_3Li phase, in a controlled manner. The size,

distribution, and volume fraction of these precipitates critically govern the alloy's final strength, ductility, and fracture behavior.

The interrelationship between these processing steps is complex. For instance, the initial grain size and chemical homogeneity after homogenization influence the recrystallization behavior during solution treatment. Similarly, the deformation structure introduced by hot rolling provides the nucleation sites and driving force for recrystallization [14,15]. Furthermore, the presence of insoluble dispersoids can pin grain boundaries and dislocations, thereby affecting both recrystallization kinetics and precipitation dynamics [16,17]. Consequently, the processing route is not merely a sequential application of treatments but a strategic design of the material's microstructure across multiple length scales, from the macroscopic grain structure down to the nano-scale precipitate distribution.

Despite the recognized importance of processing, a significant scientific gap remains: most existing studies on Al-Li-Mg alloys focus either on the final properties of fully processed materials or on the effect of isolated processing parameters. A systematic investigation that tracks the entire processing route—from the as-cast state through homogenization, hot rolling, solution treatment, to peak aging—and explicitly links each stage to specific microstructural changes and the consequent evolution of mechanical properties has been lacking, especially for alloys tailored to lightweight sports equipment applications. To address this gap, this work systematically investigates the effect of a specific processing route, comprising homogenization, hot rolling, solution treatment, and peak aging, on the microstructure and mechanical properties of an Al-Li-Mg alloy intended for sports equipment. The novelty lies in providing a comprehensive, stage-by-stage analysis of the processing–microstructure–property relationship. Unlike prior reports, we systematically characterize the microstructural transformations (grain structure, intermetallic phase dissolution/fragmentation, recrystallization, and nanoscale precipitation) induced by each processing step and quantitatively correlate them with the dramatic enhancement in mechanical properties. This integrated approach not only reveals how each processing stage contributes to the final property profile but also offers practical guidelines for the thermomechanical design of high-performance, lightweight Al-Li-Mg alloys that meet the stringent performance requirements of the sports equipment industry.

2. Experimental Materials and Methods

2.1. Materials Synthesis

The Al-Li-Mg alloy was produced in a laboratory setting at Central South University. High-purity raw materials (Al, Li, Mg, each with a purity of 99.99%) supplied by Changsha Ximingte New Material Co., Ltd. (Changsha, China) were melted in an electric resistance furnace at 760 °C under a protective argon atmosphere to prevent oxidation. After complete melting, the melt was continuously stirred to ensure homogeneous distribution of alloying elements, and then held at 720 °C for approximately 10 min. Subsequently, the molten metal was poured into a water-cooled copper mold, preheated to 200 °C, and left to cool to room temperature in air. The chemical composition of the as-cast alloy was determined by inductively coupled plasma optical emission spectrometry (ICP-OES), as listed in Table 1.

Table 1. ICP-OES-measured chemical compositions.

	Li	Mg	Fe	Si	Al
wt.% (mass percentage)	2.56	2.91	0.12	0.10	Bal.
at.% (atomic percentage)	9.20	3.00	0.054	0.09	Bal.

The as-cast ingot then underwent the following sequential processing steps: (i) Homogenization: two-step treatment in air—first at 420 °C for 8 h, followed by 500 °C for 16 h, then air-cooled to room temperature; (ii) Hot rolling: the homogenized material was reheated to 450 °C at 10–15 °C/min, held for 4 h, then hot-rolled in three sequential passes to a final thickness of 2 mm, with air cooling after each pass; (iii) Solution treatment: the rolled sheet was solution heat-treated at 500 °C for 40 min and then rapidly quenched in water; and (iv) Isothermal aging: performed at 160 °C for various durations (0–48 h) to obtain the peak-aged condition (as determined from the age-hardening curve). All thermal processing parameters were selected based on prior experimental work on Al alloys.

2.2. Characterization Techniques

The specimens were cut from the central zone of the ingot for microstructural characterization, phase identification, and mechanical testing.

Microstructural characterization was performed using optical microscopy (OM, POLYVAR-METHMV-2, Reichert-Jung, Copenhagen, Denmark), scanning electron microscopy (SEM, TESCAN MIRA3, TESCAN, Brno, Czech Republic), and transmission electron microscopy (TEM, FEI Talos F200X G2, Thermo Fisher Scientific, Hillsboro, OR, USA). Elemental distribution was assessed via energy-dispersive X-ray spectroscopy (EDS) integrated with the SEM system. Grain size analysis was performed on anodized OM images using Image-Pro Plus software (Media Cybernetics Inc., Rockville, MD, USA). The specimens for the OM and SEM observations were prepared using standard metallographic preparation, including mechanical grinding and polishing. For OM observation, to enhance grain boundary visibility, polished surfaces underwent anodization in an electrolyte comprising fluoroboric acid and distilled water at a volume ratio of 1:19, utilizing a TPR-6405D DC power supply set to 20 V and 0.1 A. For SEM observation, polished surfaces were etched with 2% nital solution. TEM foil preparation began with mechanical thinning to around 70 μm, after which 3 mm diameter discs were punched. These discs were then electropolished using a twin-jet apparatus with a 1:3 volumetric mixture of HNO_3 and CH_3OH, cooled to between −40 °C and −30 °C via a liquid nitrogen system.

Phase identification was performed using X-ray diffraction (XRD, D/max 2550, Rigaku Inc., Tokyo, Japan). XRD was conducted using Cu Kα radiation (40 kV, 30 mA) at a scan rate of 8 °/min.

Mechanical testing was performed using Vickers hardness testing and tensile testing. Vickers microhardness measurements were conducted on an HV-1000 instrument (Shimadzu HMV-G, Shimadzu, Tokyo, Japan) using a 200 gf load applied for 15 s. The final hardness values reported are averages derived from a minimum of ten random indentations per specimen. The tensile experiment was performed at room temperature with a constant crosshead speed of 2 mm/min using an electronic universal tensile test machine (MTS810, MTS Systems Corporation, Eden Prairie, MN, USA) according to the ASTM E8M standard [18]. The fracture morphologies of the specimens after the tensile test were examined by SEM.

3. Results

Figure 1a,b show optical micrographs of the as-cast alloy ingot, with Figure 1b presenting a higher-magnification image. The as-cast microstructure was characterized by large α-Al grains with prominent dendritic structures and a coarse, non-continuous network of IMCs decorating the grain boundaries. Some black micro-pores, which are common casting defects, were also observed. Figure 1c shows a corresponding anodized optical micrograph. Under polarized light, different grains exhibit distinct colors, enhancing contrast and allowing clearer differentiation of the grain structure, which consists primarily of essentially

equiaxed α-Al grains. The corresponding grain size distribution is shown in Figure 1d, which follows a Gaussian distribution with an average grain size of approximately 200 μm. Micro-pores are also clearly visible along the α-Al grain boundaries in the anodized image. These microstructural features are consistent with typical as-cast Al alloy microstructures.

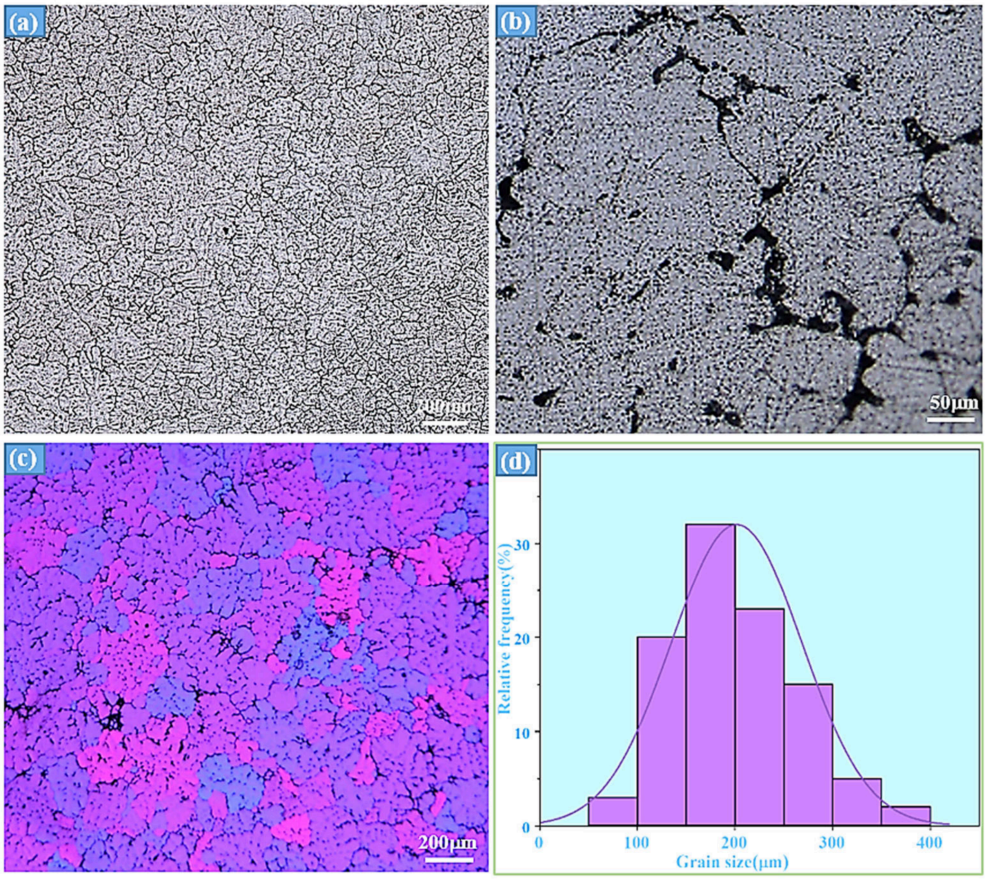


Figure 1. (**a**) Optical micrograph, (**b**) Higher-magnification image of (**a**), (**c**) Anodized optical micrograph, (**d**) Grain size distribution of as-cast alloy ingot.

Figure 2 shows the XRD patterns of the as-cast alloy ingot. The diffraction peaks correspond exclusively to the α-Al, δ′-Al_3Li, and S1-Al_2MgLi phases, with no other phases detected. XRD analysis is crucial for identifying the phase constituents present in the alloy, as it provides definitive evidence of the formation of δ′-Al_3Li and S1-Al_2MgLi phases while ruling out the presence of other intermetallics. The presence of the δ′-Al_3Li peak and the absence of an AlLi peak are attributed to the Mg content in the alloy. Thermodynamic calculations have shown that with increasing Mg content, the S1-Al_2MgLi phase increased while the AlLi phase decreased [4]. The Mg content (2.91 wt.%) in the present alloy is sufficient to suppress the formation of the AlLi phase.

Figure 3 shows the SEM-EDS results of the as-cast alloy ingot, comprising the SEM micrograph (Figure 3a) and the corresponding elemental distribution maps for layered elements, Al, Mg, Fe, and Si (Figure 3b–f). SEM combined with EDS is essential for characterizing the morphology, distribution, and chemical composition of intermetallic compounds and residual phases, especially when the phases are too coarse for XRD to resolve their spatial heterogeneity. The SEM image in Figure 3a reveals that the microstructure consists of α-Al grains and primary IMCs. The primary IMCs are mainly located along or adjacent to the boundaries of the α-Al grains, exhibiting a somewhat non-continuous net-like distribution. The EDS-determined compositions of Points 1 and 2, marked in Figure 3a, are summarized in Table 2. Point 1 corresponds to the α-Al matrix, whereas

Point 2 is situated within the network of primary IMCs distributed along and adjacent to the α-Al grain boundaries. Analysis reveals that Point 1 consists predominantly of Al with approximately 2.3 at.% Mg. In contrast, Point 2 is enriched in Al, contains approximately 24.4 at.% Mg and 1.8 at.% Fe, and corresponds to the primary IMCs. Notably, due to the low atomic number of Li and the consequent strong absorption of its characteristic X-rays, its distribution could not be detected by EDS [19–21]. The maps (Figure 3b–f) clearly show significant co-segregation of Mg and Fe within the grain-boundary IMCs, with their enriched regions largely overlapping. Si enrichment is only observed locally at grain-boundary ends, suggesting the possible formation of Mg_2Si. In conjunction with the XRD results and EDS data, the Mg-rich primary IMCs forming the discontinuous network in Figure 3a are identified as the S1-Al_2MgLi phase, which also shows segregation of the impurity element Fe.

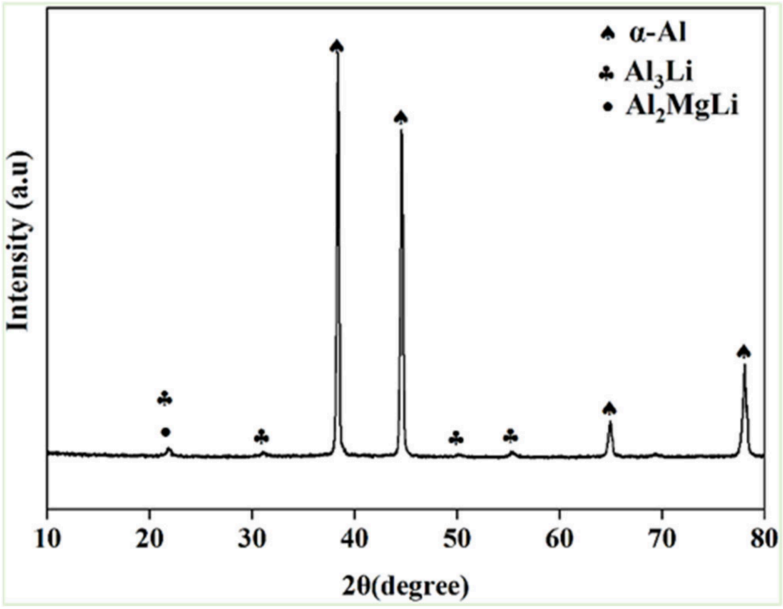


Figure 2. XRD pattern of as-cast alloy ingot.

Table 2. EDS-determined compositions of Points 1 and 2 (at.%), marked in Figure 3a.

	Mg	Fe	Si	Al
1	2.31	0.00	0.13	97.56
2	24.43	1.78	0.26	73.53

Figure 4a shows the anodized optical micrograph of the homogenized alloy ingot. Most of the non-equilibrium phases at the grain boundaries have dissolved back into the matrix. This indicates that the homogenization eliminated or reduced the compositional heterogeneity of the as-cast microstructure, which is beneficial for improving the formability of the alloy and preparing a suitable microstructure for subsequent hot working. Compared to the as-cast condition, the grains exhibited slight coarsening after homogenization, with an average size of approximately 230 μm. The corresponding grain size distribution, which follows a Gaussian distribution, is shown in Figure 4b. However, as homogenization cannot eliminate casting defects, some micro-voids remained in the alloy. Figure 4c–h show the corresponding SEM-EDS results, comprising the SEM micrograph (Figure 4c) and the elemental distribution maps for layered elements, Al, Mg, Fe, and Si (Figure 4c–h). The SEM image in Figure 4c reveals that while most of the solidified phases had dissolved into the matrix, a considerable amount of bright residual phases persisted, presenting a

discontinuous distribution. The maps (Figure 4d–h) clearly show that the segregation of Mg is largely eliminated, with Mg becoming uniformly distributed within the α-Al matrix. Impurity Fe is segregated at the remaining bright particles, while a slight enrichment of Mg is observed at sites where Si is concentrated, suggesting the possible formation of Mg_2Si phase. This indicates that the residual phases after homogenization are high-melting-point intermetallics containing Fe and Si, which are difficult to dissolve through the homogenization.

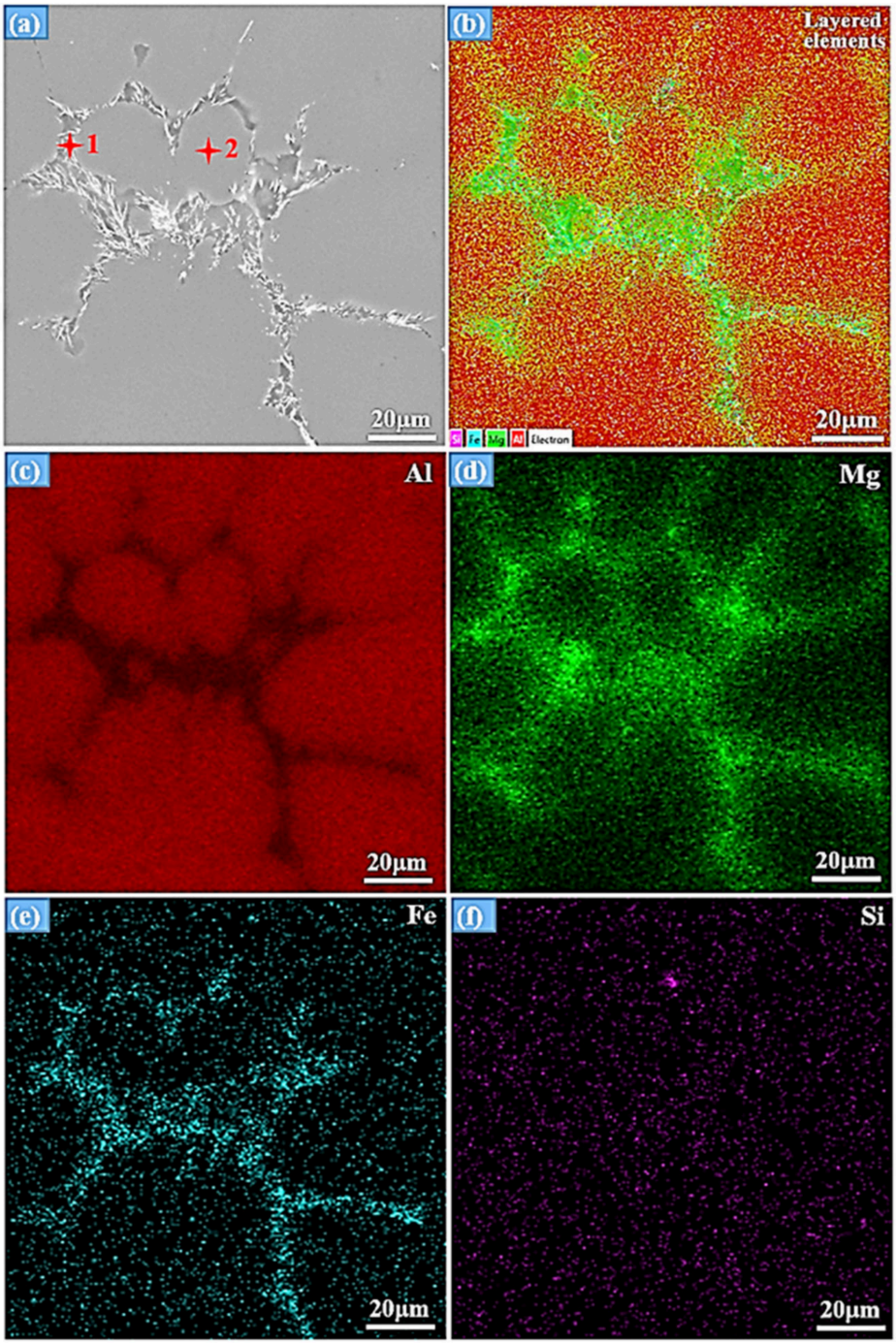


Figure 3. SEM-EDS results of as-cast alloy ingot: (**a**) SEM micrograph, and (**b**–**f**) Corresponding elemental distribution maps for layered elements, Al, Mg, Fe, and Si.

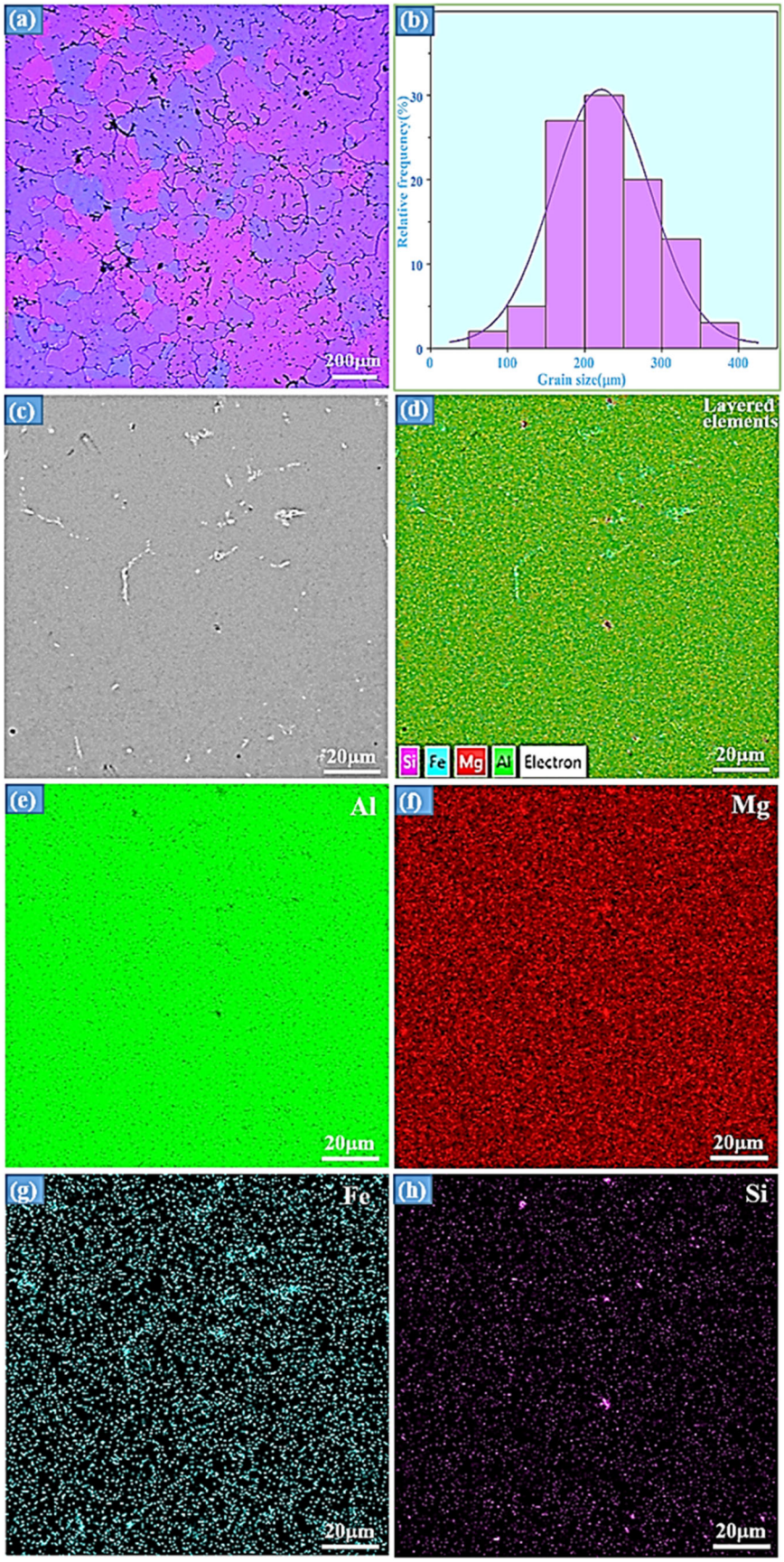


Figure 4. (**a**) Anodized optical micrograph, (**b**) Grain size distribution, (**c**) SEM micrograph, (**d**–**h**) Corresponding elemental distribution maps for layered elements, Al, Mg, Fe, and Si of homogenized alloy ingot.

Figure 5a shows the anodized optical micrograph of the hot-rolled alloy ingot, viewed along the rolling direction–normal direction (RD-ND) plane. Plastic deformation during rolling led to pancake-shaped or lamellar grains, creating a pronounced fibrous texture along the rolling axis. In conventional Al alloys, hot rolling typically induces dynamic recovery or recrystallization, which would partially recrystallize such deformed fibrous grains [22,23]. However, no obvious recrystallized grains were observed here, indicating that dynamic recovery, rather than dynamic recrystallization, was the dominant mechanism during hot rolling in the present alloy. The fibrous structures introduced by this severe plastic deformation are expected to provide a favorable condition for subsequent recrystallization during solution treatment. Figure 5b shows a corresponding SEM micrograph. The second-phase particles are aligned along the rolling direction, exhibiting a distinct yet discontinuous streamline distribution. Based on the analysis of residual phases after homogenization mentioned above, these particles can be identified as undissolved high-melting-point phases containing Fe and Si. The hot rolling process fractured these coarse residual particles, leading to a more uniform distribution within the matrix, which mitigates their detrimental effect on alloy properties. A detailed analysis of these second-phase particles will be provided subsequently.

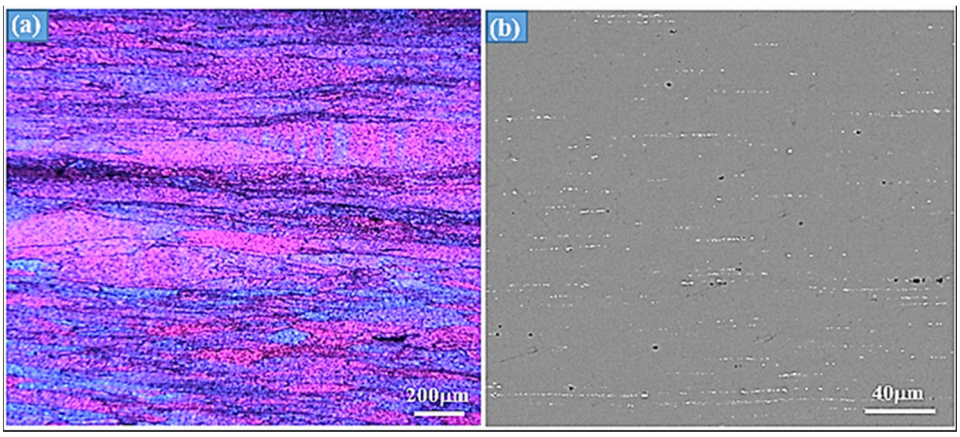


Figure 5. (**a**) Anodized optical micrograph, (**b**) SEM micrograph of hot-rolled alloy ingot.

Figure 6a shows the anodized optical micrograph of the solution-treated alloy ingot, viewed along the rolling direction. The microstructure consists of nearly equiaxed grains with an average size of ~150 μm, indicating that the fibrous morphology was fully eliminated and complete recrystallization occurred. The corresponding grain size distribution, which follows a Gaussian distribution, is shown in Figure 6b. Figure 6c–h show the corresponding SEM-EDS results, comprising the SEM micrograph (Figure 6c) and the elemental distribution maps for layered elements, Al, Mg, Fe, and Si (Figure 6d–h). Some of the second-phase particles fragmented during rolling were dissolved back into the matrix, while undissolved particles persisted, aligned in discontinuous streamlines along the rolling direction (Figure 6c). These remnants exhibited a relatively distinct, discontinuous distribution and appeared as finely fragmented precipitates with a brighter contrast compared to the matrix. The compositions of Points 3 and 4 in Figure 6c are listed in Table 3, based on EDS data. Point 3 represents a position within the matrix, and Point 4 corresponds to a finely fragmented precipitate, with the latter exhibiting bright contrast. The EDS results indicated that Point 3 contained 0 at.% Fe and Point 4 contained 5.7 at.% Fe. The corresponding elemental distribution maps for the region in Figure 6c, showing the layered image and the distributions of Al, Mg, Fe, and Si, are presented in Figure 6d–h, respectively. These undissolved particles, with high melting points, persisted through both homogenization and solution treatment. EDS data confirmed that these residual particles

were primarily enriched in Fe, identifying them as Al-Fe-based compounds. Additionally, regions showing co-segregation of Mg and Si suggested the formation of Mg_2Si phases.

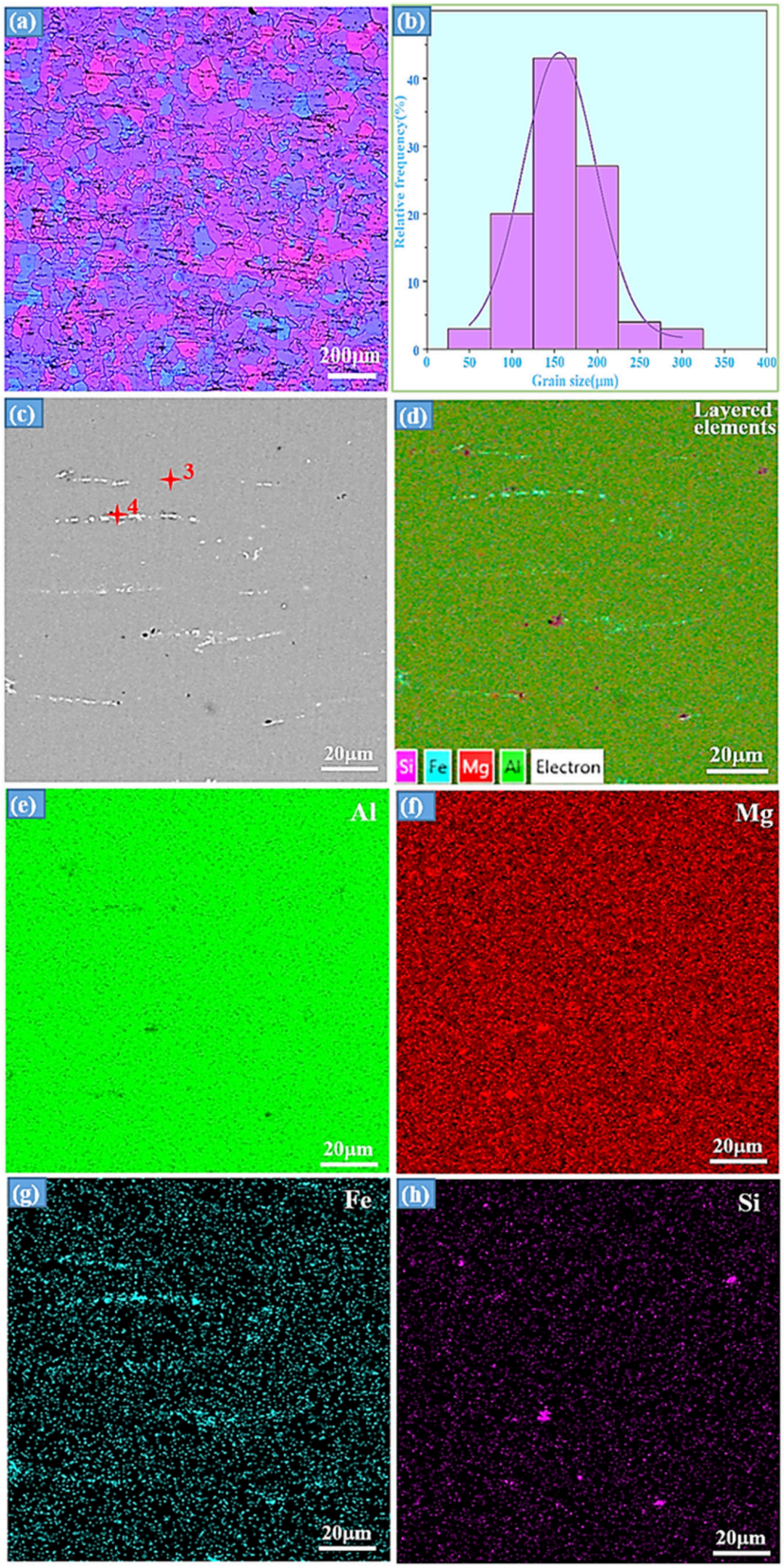


Figure 6. (**a**) Anodized optical micrograph, (**b**) Grain size distribution, (**c**) SEM micrograph, (**d**–**h**) Corresponding elemental distribution maps for layered elements, Al, Mg, Fe, and Si of solution-treated alloy ingot.

Table 3. EDS-determined compositions of Points 3 and 4 (at.%), marked in Figure 6c.

	Mg	Fe	Si	Al
3	3.28	0.00	0.24	96.48
4	2.98	5.68	0.19	91.15

Figure 7a shows the Vickers hardness (HV) of the aged alloy ingot as a function of aging time (t). The age-hardening curve demonstrates a rapid initial increase in hardness during the first 2 h of aging. This is followed by a period of more gradual hardening until a peak value of approximately 133 HV was attained after 24 h. After the peak, the hardness decreases slightly and then stabilizes with further aging. Figure 7b shows the room-temperature engineering tensile stress–strain curves for the as-cast and peak-aged specimens. Both curves exhibit nearly continuous yielding without a distinct yield point. After an initial linear elastic region, plastic deformation begins, marked by a gradual change in slope. The stress rises steeply in the elastic stage, indicating a high elastic modulus. Upon yielding, strain hardening is rapid at first and then decreases to a lower rate during subsequent plastic deformation until the stress reaches a maximum and fracture occurs. Room-temperature tensile testing reveals a dramatic enhancement in mechanical performance after the full processing route. The peak-aged alloy exhibits a yield strength (YS) of ~265 MPa, an ultimate tensile strength (UTS) of ~390 MPa, and an elongation (EL) of ~20.5%. This represents a substantial improvement over the as-cast alloy, which has corresponding values of ~138 MPa, ~163 MPa, and ~2.1%, translating to increases of approximately 92%, 139%, and 925%, respectively.

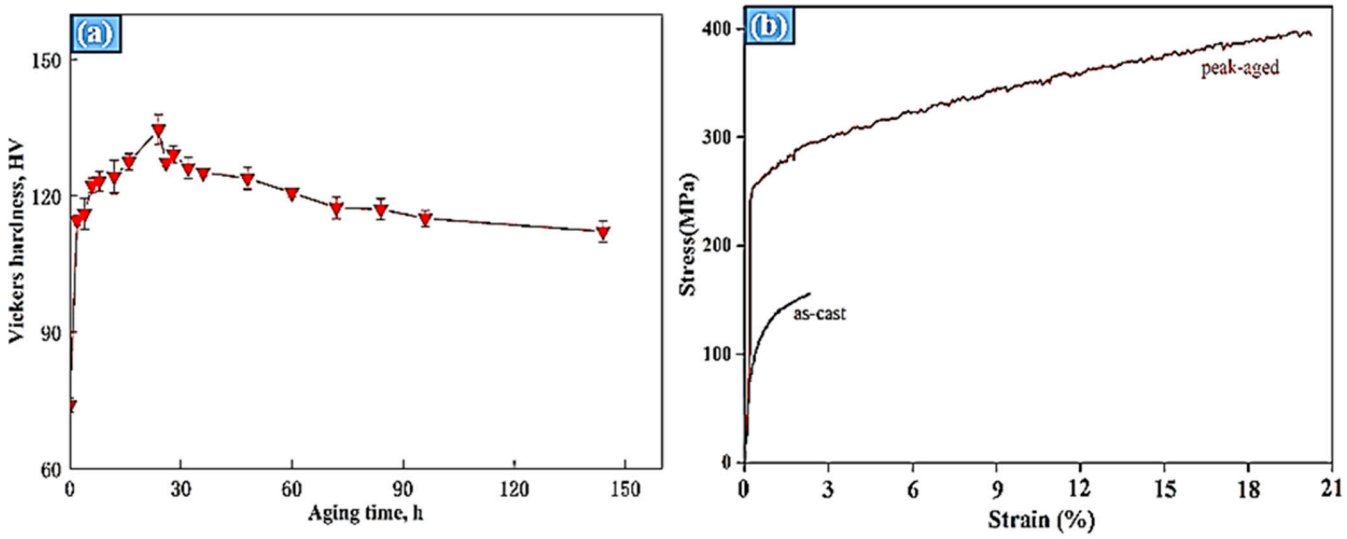


Figure 7. (**a**) Age-hardening curve (HV vs. aging time at 160 °C) of aged alloy, (**b**) Engineering tensile stress–strain curves at room temperature for as-cast condition and peak-aged condition.

Figure 8 presents SEM fractographs of the tensile specimens after room-temperature testing. The as-cast specimen (Figure 8a) exhibits a predominantly intergranular fracture surface, while the peak-aged specimen (Figure 8b) shows a small, shallow dimpled morphology characteristic of ductile fracture. Fractographic examination provides insights into the corresponding fracture mechanisms. The as-cast tensile specimen features a fracture surface characteristic of intergranular failure, consistent with the presence of the brittle, continuous network of IMCs at the grain boundaries. In contrast, the fracture surface of the peak-aged specimen shows fine, shallow dimples. This morphology is characteristic of

ductile fracture via microvoid coalescence, indicating substantial plastic deformation prior to failure and corroborating the observed increase in ductility [24,25].

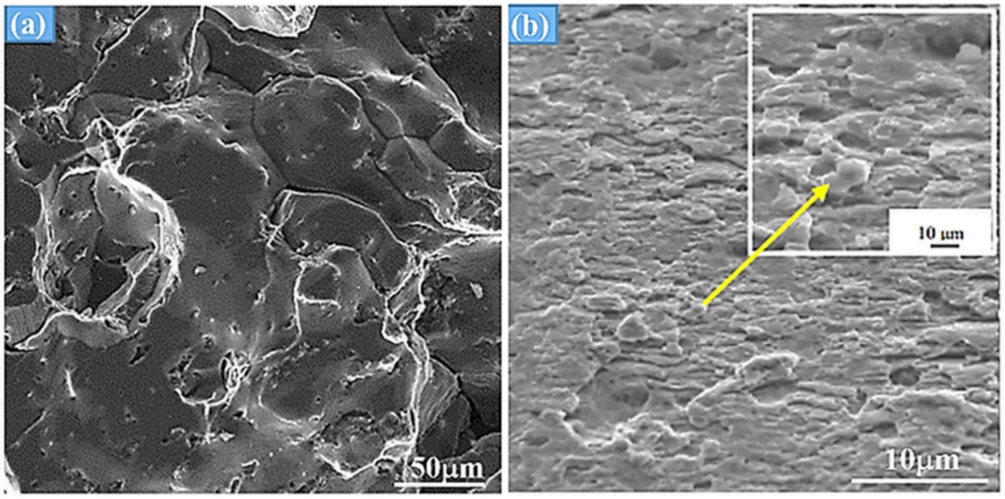


Figure 8. SEM fractographs of tensile specimens: (**a**) As-cast specimen, (**b**) Peak-aged specimen.

4. Discussion

This study into the influence of the processing route on the Al-Li-Mg alloy reveals a complex interaction between thermal and mechanical treatments and the resultant microstructural evolution, which directly influences the final mechanical properties. The evolution from the coarse, heterogeneous as-cast structure to the refined, strengthened peak-aged condition highlights the critical importance of each sequential processing stage in tailoring the material for high-performance sports equipment applications, where an optimal combination of strength, ductility, and light weight is essential.

The initial as-cast microstructure serves as the foundational state upon which all subsequent modifications are applied. The presence of coarse, equiaxed α-Al grains with an average size of approximately 200 μm, accompanied by a dendritic network and a coarse, discontinuous intermetallic network along grain boundaries, is characteristic of conventional casting solidification. The identification of this network as the S1-Al_2MgLi phase, enriched with impurity Fe, is significant. The thermodynamic suppression of the AlLi phase in favor of S1-Al_2MgLi due to the specific Mg content establishes the initial phase constituents [4]. This grain boundary network, combined with observed micro-porosity, inherently compromises mechanical integrity. The brittle nature of these discontinuous intermetallics provides easy crack propagation paths, as confirmed by the intergranular fracture mode and the minimal EL of approximately 2.1% in the as-cast tensile tests. This microstructure is fundamentally unsuitable for any structural application requiring appreciable toughness or formability.

The application of homogenization represents the first critical step in microstructural modification, aimed at reducing chemical segregation inherited from solidification. The dissolution of the majority of the non-equilibrium S1-Al_2MgLi phase back into the α-Al matrix is clear evidence of reduced compositional heterogeneity. This redistribution of Mg, transforming it from a segregated grain boundary constituent to a more uniform solute within the matrix, is essential for enhancing homogeneity and improving subsequent workability. The slight grain coarsening observed, from 200 μm to 230 μm, is a typical thermal effect where grain boundary migration occurs to reduce interfacial energy. However, the persistence of bright residual phases after homogenization highlights a key limitation of this treatment. These phases, identified as high-melting-point intermetallics containing Fe and Si (and likely forming compounds such as Al-Fe-Si or Mg_2Si), remain stable and

undissolved. Their presence is attributed to the low solid solubility and slow diffusion kinetics of these impurity elements in the α-Al matrix at homogenization temperatures. Consequently, while homogenization successfully addresses the macro-segregation of the primary alloying elements (Mg and Li), it is ineffective against the micro-segregation of certain impurities, leaving behind dispersion of thermally stable particles. These residual particles, though discontinuous, will play a defining role in subsequent processing stages.

Hot rolling introduces severe plastic deformation, fundamentally changing the micro-morphology. The transformation of the equiaxed grains into a pronounced fibrous or pancake-shaped structure aligned with the rolling direction is a direct consequence of the imposed strain. Notably, the absence of obviously dynamically recrystallized grains suggests that dynamic recovery was the predominant restoration mechanism during hot working in this specific alloy composition. The high stacking fault energy of Al alloys typically favors recovery over recrystallization [26,27]. Furthermore, the presence of finely dispersed precipitates or solute atoms, such as those from the dissolved and re-precipitated phases, can pin subgrain boundaries and suppress the nucleation and growth of new recrystallized grains during deformation [28,29]. The alignment of the undissolved high-melting-point particles into a streamlined distribution along the rolling direction is another significant result. The rolling process fragments these coarse, brittle residual particles, reducing their size and spacing. This fragmentation is beneficial as it mitigates the stress-concentrating effect of large, blocky particles that are often detrimental to ductility and fracture toughness. The deformed, unrecrystallized fibrous structure, with its high density of dislocations and subgrain boundaries, stores a substantial amount of strain energy [30]. This stored energy provides a potent driving force for subsequent static recrystallization during the subsequent solution treatment, setting the stage for grain refinement.

The solution treatment following hot rolling is critical in achieving a fully recrystallized, equiaxed grain structure. The complete replacement of the deformed fibrous grains with nearly equiaxed grains averaging 150 μm in size indicates successful static recrystallization. The driving force for this recrystallization stems primarily from the strain energy stored within the deformed matrix during hot rolling. The recrystallized grain size, being finer than the initial as-cast and homogenized grain sizes, demonstrates the potential of deformation-assisted thermo-mechanical processing for grain refinement. Concurrently, the solution treatment aims to take the alloying elements, particularly Li and Mg, into solid solution within the α-Al matrix to prepare for age hardening. However, the microstructural analysis indicates that the streamlined distribution of the fragmented Fe- and Si-containing particles persists even after this treatment. Their stability confirms their high melting point and low solubility, making them unaffected by the solutionizing temperature. They remain as dispersed, incoherent second-phase particles within the recrystallized matrix. The cooling stage from the solution treatment temperature is critical, as it initiates the precipitation sequence for the age-hardening phases.

The precipitation behavior, particularly of the δ′-Al_3Li phase, is key to the alloy's strengthening mechanism. TEM combined with selected area electron diffraction (SAED) is indispensable for revealing nanoscale precipitates and their crystal structure, which directly governs the strengthening mechanism. The TEM image in the peak aging condition reveals a homogeneous dispersion of nanoscale precipitates with an average diameter of 9.9 ± 2.3 nm (Figure 9a). The corresponding SAED patterns display distinct $L1_2$ superlattice reflections alongside the fundamental spots from the α-Al matrix, confirming these precipitates as the δ′-Al_3Li phase (Figure 9b). The low interfacial energy associated with the coherent δ′-Al_3Li phase facilitates its homogeneous nucleation throughout the matrix. The identification of the strengthening mechanism depends on the interaction between moving dislocations and these precipitates. For the δ′-Al_3Li phase, two primary strengthening

mechanisms operate: (i) dislocation shearing, in which dislocations cut through coherent precipitates, and (ii) Orowan looping, in which dislocations bypass non-shearable particles by bowing around them. The critical transition radius is reported to be around 25 nm for the Al_3Li system [31]. Given the average radius of approximately 5 nm in the peak-aged condition, it is substantially below this threshold. Therefore, the predominant strengthening mechanism in this alloy is concluded to be dislocation shearing. This mechanism involves the creation of a new particle–matrix interface as the dislocation passes through, and the energy required for this process, combined with possible modulus and coherency strain effects, contributes significantly to the increase in YS. The uniform distribution ensures that dislocation motion is inhibited throughout the matrix, leading to effective strengthening.

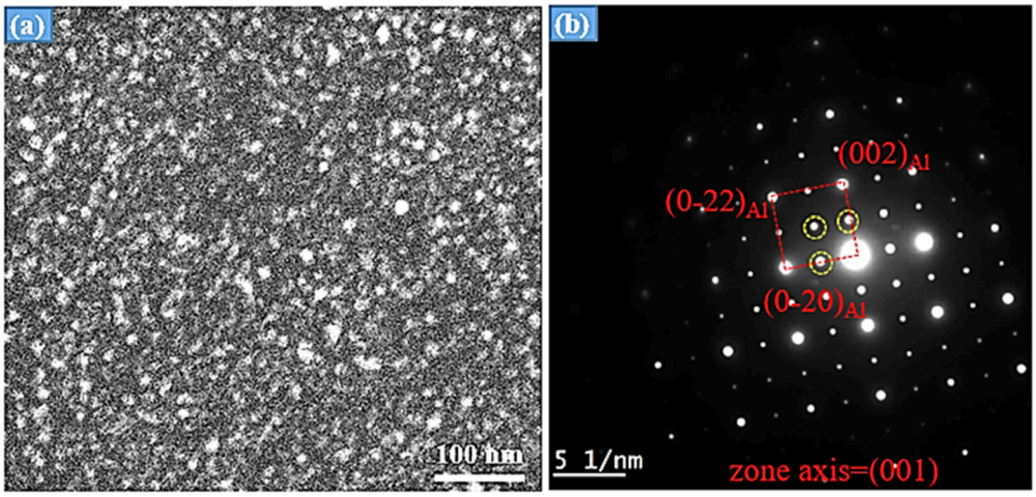


Figure 9. (**a**) TEM image, (**b**) Corresponding SAED pattern for peak aging condition.

The combined use of XRD, SEM/EDS, and TEM/SAED provides a comprehensive, multi-scale understanding of microstructural evolution from macroscopic phase identification (XRD) and micrometric elemental distribution (SEM/EDS) to nanometric precipitate characterization (TEM/SAED). This hierarchical approach is critical for establishing the processing–microstructure–property relationship, as it allows each processing stage to be correlated with specific microstructural changes across length scales.

The dramatic enhancement in mechanical properties from the as-cast to the peak-aged state is the most direct evidence of the efficacy of the applied processing route. The increases of approximately 92% in YS, 139% in UTS, and an extraordinary 925% in EL collectively represent a transformation from a brittle, low-strength casting to a strong and ductile processed alloy. This transformation can be decomposed into the contributions from various microstructural features tailored through processing. The elimination of the continuous, brittle S1-Al_2MgLi grain boundary network via homogenization and its replacement by a uniform solution treatment is a fundamental requirement for improved ductility. The hot rolling process, while not inducing recrystallization itself, refines the microstructure by elongating grains and, more importantly, by fragmenting the coarse, harmful impurity phases. This fragmentation reduces their effective size and improves their distribution, diminishing their role as crack nucleation sites. The subsequent solution treatment achieves complete recrystallization, resulting in a fine, equiaxed grain structure free of deformation textures. Grain boundaries act as barriers to dislocation motion, contributing to strength via the Hall–Petch relationship [32,33], and a fine grain size typically enhances ductility as well [34–36]. Finally, and most significantly, the age-hardening response through the precipitation of the fine, coherent δ'-Al_3Li phase provides the major enhancement in strength [37,38]. The shearing of these precipitates by dislocations provides

a strong but accommodable barrier to plastic flow, allowing for substantial strain hardening and a high UTS while maintaining good ductility. The transition in fracture mode from intergranular in the as-cast state to a dimpled, ductile rupture in the peak-aged condition provides microscopic corroboration of this property enhancement. The shallow dimples are often associated with the nucleation of microvoids at second-phase particles (likely the fragmented Fe/Si-containing particles) and their subsequent growth and coalescence, a process requiring plastic deformation of the surrounding matrix.

The persistence of Fe- and Si-containing phases throughout the entire processing sequence necessitates further consideration. While their fragmentation and more uniform distribution mitigate their worst effects, they remain as intrinsic microstructural features. In the context of sports equipment, where fatigue resistance and fracture toughness are often critical, the role of such insoluble particles is ambiguous. On one hand, finely dispersed, hard particles can impede dislocation movement and contribute to strength. On the other hand, they can act as stress concentrators and potential sites for fatigue crack initiation, especially if they exist in clusters or retain sharp corners post-fragmentation. The observed slight enrichment of Mg at Si-rich sites, suggesting Mg_2Si formation, also indicates that these impurity elements can interact with the primary alloying elements, potentially tying up some Mg that would otherwise be available for solid solution strengthening or participation in other precipitation reactions. This underscores the importance of raw material purity in alloys designed for maximum performance, as the processing route can mitigate but not eliminate the detrimental effects of certain impurities.

Overall, the processing route comprising homogenization, hot rolling, solution treatment, and peak aging facilitates a series of microstructural transformations that collectively tailor the desired properties in the Al-Mg-Li alloy. The sequence successfully addresses the deficiencies of the cast structure by homogenizing chemistry, refining grain structure, managing insoluble impurities, and, most effectively, introducing a dense dispersion of coherent strengthening precipitates. The dominant strengthening mechanism is identified as dislocation shearing through the δ'-Al_3Li precipitates. The result is a material that achieves a superior balance of strength and ductility, making it a promising candidate for lightweight, high-strength components in sports equipment. The findings highlight that the properties are not merely a function of composition but are profoundly governed by the thermo-mechanical history, which controls the character, distribution, and scale of all microstructural constituents from the grain architecture down to the nanoscale precipitates.

5. Conclusions

This work systematically investigates the effect of a specific processing route, comprising homogenization, hot rolling, solution treatment, and peak aging, on the microstructure and mechanical properties of an Al-Li-Mg alloy intended for sports equipment. The novelty lies in the first systematic, stage-by-stage tracking of microstructural evolution from as-cast to peak-aged condition in this alloy system, quantitatively linking each processing step to the final property enhancement for lightweight sports equipment applications. The main findings are summarized as follows:

1. The processing route effectively transforms the coarse, heterogeneous as-cast microstructure into a refined, fully recrystallized grain structure with a uniform dispersion of nanoscale δ'-Al_3Li precipitates, demonstrating the critical role of thermo-mechanical control in tailoring microstructural features.
2. A significant enhancement in mechanical performance is achieved through the applied processing sequence, with the peak-aged alloy exhibiting a superior combination of strength and ductility compared to the as-cast condition: approximately a 92% increase in YS, a 139% increase in UTS, and an exceptional 925% increase in EL. This

improvement is attributed to the synergistic effects of grain refinement, dissolution of brittle intermetallics, and controlled precipitation of strengthening phases.

3. The dominant strengthening mechanism in the peak-aged condition is dislocation shearing of coherent δ'-Al_3Li precipitates, which effectively impedes dislocation motion while preserving ductility. The fracture behavior transitions from brittle intergranular failure in the as-cast state to ductile microvoid coalescence after processing, consistent with the observed microstructural evolution.
4. Although the processing route mitigates the harmful effects of impurity phases containing Fe and Si through fragmentation and redistribution, their persistence underscores the importance of raw material purity in optimizing alloy performance. The final properties of Al-Li-Mg alloys are governed not only by composition but also by the strategic design of the processing sequence across multiple microstructural scales.

Author Contributions: Conceptualization, G.L., Y.Z. (Yuncheng Zhu) and M.-C.Z.; Methodology, D.Y.; Software, Y.Z. (Yingchao Zhao); Formal analysis, S.Z. and X.L.; Investigation, S.Z.; Resources, D.Y.; Data curation, G.L., S.Z., X.L. and Y.Z. (Yingchao Zhao); Writing—original draft, G.L.; Writing—review & editing, M.-C.Z.; Visualization, Y.Z. (Yuncheng Zhu) and X.L.; Project administration, M.-C.Z.; Funding acquisition, M.-C.Z. All authors have read and agreed to the published version of the manuscript.

Funding: Financially supported by Large Aircraft Advanced Materials Innovation Alliance Project, Project Number IAAAM202201001.

Data Availability Statement: The original contributions presented in the study are included in the article, further inquiries can be directed to the corresponding author.

Conflicts of Interest: The authors declare no conflicts of interest.

References

1. Leng, B.; Xue, Y.H.; Li, J.; Qi, J.T.; Yi, A.H.; Zhao, Q.X. A critical review of anti-corrosion chemical surface treatment of aluminum alloys used for sports equipment. *Crystals* **2024**, *14*, 101. [CrossRef]
2. Wang, Y.Q.; Huang, F.; Qian, X.Z. MoTiCo conversion coating on 7075 aluminium alloy surface: Preparation, corrosion resistance analysis, and application in outdoor sports equipment trekking poles. *Metals* **2025**, *15*, 864. [CrossRef]
3. Wang, Y.Q.; Qian, X.Z.; Huang, F.; Fang, Y.S. Preparation of new vanadium base composite conversion coating on 6061 aluminum alloy surface for sports equipment. *Coatings* **2025**, *15*, 516. [CrossRef]
4. Strarke, E.A.; Sanders, T.H.; Palmer, I.G. New approaches to alloy development in the Al-Li system. *JOM* **1981**, *33*, 24–33. [CrossRef]
5. Shi, C.C.; Wu, G.H.; Zhang, L.; Zhang, X.X.; Sun, J.W.; Zhang, J.S. Microstructures and mechanical properties of ultralight cast Al-3Li-XMg-0.1Zr alloys. *Mater. Charact.* **2020**, *170*, 110698. [CrossRef]
6. Peng, M.L.; Xiao, D.H.; Liu, W.S. Optimizing microstructure and mechanical properties of 2195 Al-Li alloy via thermomechanical treatment: Precipitate regulation mechanism. *J. Mater. Res. Technol.* **2026**, *40*, 4028–4046. [CrossRef]
7. Yin, D.; Zhang, S.; Li, X.; Yao, J.A.; Yin, Q.; Atrens, A.; Zhao, M. Insights into core-shell multi-structure and strengthening by multi-microalloying (Sc, Zr, Er and Ti) of a T6 treated Al-Li-Mg alloy. *J. Mater. Res. Technol.* **2025**, *34*, 286–296. [CrossRef]
8. Mogucheva, A.; Kaibyshev, R. Microstructure and Mechanical Properties of an Al-Li-Mg-Sc-Zr Alloy Subjected to ECAP. *Metals* **2016**, *6*, 254.
9. Wang, W.H.; Pan, X.L.; He, P.; Xie, L.; Tian, B.S.; Li, B.; Yang, H.W.; Fu, Y.; He, Y.; Shen, Q.Y.; et al. Review of short-to-ultrashort pulsed laser shock peening research: Mechanisms, processes, and applications. *Int. J. Extrem. Manuf.* **2026**, *8*, 032014. [CrossRef]
10. Zhang, Y.Q.; Zhan, M.; Fan, X.G.; Li, H.W. The interaction among deformation, precipitation/precipitates, and properties of 2219 aluminum alloy tubes under complex thermo-mechanical paths of solution treatment-deformation-aging. *J. Mater. Res. Technol.* **2025**, *38*, 352–366. [CrossRef]
11. Liu, J.H.; Feng, P.F.; Ji, H.S.; Zhang, J.F.; Zhang, X.Y.; Wang, J.J. Tip-based vibration carving of shape-customized convex microstructures: Principle, modeling, and experiments. *Int. J. Extrem. Manuf.* **2026**, *8*, 025101. [CrossRef]
12. Zhi, J.M.; Guo, M.X.; Wang, L.H.; Liu, Z.Y.; Xie, L.; Kestens, L. Relationship between lattice rotation, grain boundary characteristics, texture development and formability in Al-Zn-Mg-Cu alloys. *J. Alloys Compd.* **2026**, *1057*, 186854. [CrossRef]

13. Dharavathu, R.; Shetty, K.; Muvvala, G. A study on mitigation of tunneling defects and investigation on the mechanical behavior of double-sided friction stir welded Al 2014 plates. *J. Manuf. Process.* **2026**, *159*, 460–480. [CrossRef]
14. Mahato, A.; Singh, P.P.; Bajargan, G.; Mula, S. Hot deformation behavior of a cast dual-phase CoCrFeNiAl0.7 high-entropy alloy: Validation of processing maps and microstructural characteristics. *J. Alloys Compd.* **2026**, *1050*, 185583. [CrossRef]
15. Elasheri, A.; Ghosh, A.; Parson, N.; Chen, X.G. Microstructure and texture evolution during extrusion of 6xxx aluminum alloys with Mn/Zr additions. *J. Mater. Sci.* **2025**, *60*, 22252–22269. [CrossRef]
16. Ghio, E.; Cerri, E. Optimizing post friction stir welding heat treatment in dissimilar friction stir welded 6061/AlSi10MgMn joints for electrical vehicle battery housing. *Adv. Eng. Mater.* **2026**, *28*, 2502199. [CrossRef]
17. Lypchanskyi, O.; Rigas, N.; Rogal, L.; Janus, K.; Litynska-Dobrzynska, L.; Korpala, G.; Lampke, T.; Merklein, M.; Prahl, U. Strain-induced microstructural and precipitation behavior of Al-Mg-Si-Mn alloys: Effects of Si content under controlled thermomechanical conditions. *J. Mater. Sci. Technol.* **2026**, *270*, 68–85. [CrossRef]
18. *ASTM E8/E8M-21*; Standard Test Methods for Tension Testing of Metallic Materials. ASTM International: West Conshohocken, PA, USA, 2014.
19. Saikawa, S.; Nakai, K.; Sugiura, Y.; Kamio, A. Effect of hydrogen gas content on generation of porosity in Al-Li casting alloys. *Mater. Trans. JIM* **1999**, *40*, 57–63. [CrossRef]
20. Wang, Y.; Zhang, S.; Wu, R.Z.; Turakhodjaev, N.; Hou, L.G.; Zhang, J.H.; Betsofen, S. Coarsening kinetics and strengthening mechanisms of core-shell nanoscale precipitates in Al-Li-Yb-Er-Sc-Zr alloy. *J. Mater. Sci. Technol.* **2021**, *61*, 197–203. [CrossRef]
21. Sun, X.H.; Zhang, S.C.; Wang, H.W.; Yin, D.F.; Zhao, M.C. Microstructure and precipitation evolution of a (Sc, Zr, Er, Ti) multi-microalloyed Al–Li–Mg alloy from solution treatment to peak aging. *J. Mater. Res. Technol.* **2026**, *40*, 415–426. [CrossRef]
22. Chen, Y.S.; Shu, X.D.; Yan, S.Y.; Luo, C.L.; Xia, Y.X.; Xu, H.J.; Li, Z.X.; Pater, Z.; Bulzak, T. Hot deformation behavior and microstructure evolution of Al-6.4Zn-2.2Cu-2Mg alloy. *J. Mater. Res. Technol.* **2026**, *41*, 5921–5934. [CrossRef]
23. Hasnain, K.; Zarif, M.; Kamran, J.; Iqbal, Z.; Tanvir, M.T.; Asghar, Z.; Ahmad, J. Optimization of microstructure for improved mechanical and corrosion performance through controlled composition and hot rolling of AA5052 alloy. *J. Mater. Eng. Perform.* **2026**, *35*, 17232–17252. [CrossRef]
24. Wei, Z.Z.; Li, C.; Wang, Z.Y.; Zakharov, O.; Yan, G.Y.; Li, M.F.; Geng, Y.Q. A comprehensive dynamic force model involved in grinding of B4C ceramics. *Int. J. Extrem. Manuf.* **2026**, *8*, 035103. [CrossRef]
25. Li, Q.Y.; Liu, X.Y.; Luan, Z.L.; Xia, M.; He, M.C.; Ye, Y.C. Fabrication and impact performance of nickel-based ceramic/novel high-strength and high-toughness steel graded composites. *J. Mater. Res. Technol.* **2025**, *38*, 6275–6287. [CrossRef]
26. Ehsani, B.; Jamaati, R.; Aval, H.J.; Farajollahi, R.; Javidani, M. Effect of asymmetric forward rolling (AFR) on the microstructure, texture, mechanical properties, and Portevin-Le Chatelier behavior of AA5052 alloy. *J. Mater. Res. Technol.* **2025**, *39*, 2844–2863. [CrossRef]
27. Li, E.B.; Huang, H.F.; Wei, L.L.; Han, C.; Qiu, M.; Wei, X.N.; Liang, X.X.; Xie, J.J. Effect of Sc and Zr additions on themicrostructure, mechanicalproperties, and low-cycle fatiguebehavior of Al-7Mg alloy duringannealing. *J. Alloys Compd.* **2025**, *1047*, 184938. [CrossRef]
28. Wang, K.Z.; Zhang, C.S.; Kong, X.S.; Xing, X.W.; Meng, Z.J.; Chen, L.; Chen, X.X.; Tang, J.W.; Ke, Y.B.; Zhao, G.Q. Strain-induced dynamic evolution of the T1 phase and its influence on recrystallization behavior. *Acta Mater.* **2026**, *308*, 122032. [CrossRef]
29. Xia, P.; Lin, K.D.; Hu, Y.W.; Hao, J.F.; Li, R.X.; Huang, H.L. Texture evolution and in situ investigation of recrystallization behavior in a hot-rolled Al-Zn-Mg-Cu-Zr alloy. *Materials* **2026**, *19*, 665. [CrossRef] [PubMed]
30. Huang, X.; Zhao, M.C.; Yin, Q.; Yao, J.G.; Zhao, Y.C.; Yin, D.F.; Zeng, R.C.; Yang, K.; Wen, C.; Atrens, A. Insights into biodegradable Mn-incorporated Fe-based scaffolds in orthopedics: Bridging manufacturing techniques, physicomechanical properties, and multifunctional bioapplications. *Int. J. Extrem. Manuf.* **2026**, *8*, 012011. [CrossRef]
31. Furukawa, M.; Miura, Y.; Nemoto, M. Strengthening mechanisms in Al-Li alloys containing coherent ordered particles. *Trans. Jpn. Inst. Met.* **1985**, *26*, 230–235. [CrossRef]
32. Zhou, K.X.; Wang, L.L.; Zhao, Y.H.; Jin, S.B.; Mao, Q.Z.; Shi, S.J.; Ma, L.L.; Zhang, R.S.; Liu, J.Z. Strong and thermally stable nanocrystalline Cu-Al alloy via Al segregation. *Int. J. Extrem. Manuf.* **2025**, *7*, 025101. [CrossRef]
33. Wang, Y.X.; Ji, Y.; Yang, B. Interface-dominated toughening mechanism in yttrium-modified Cr-Mo-V steel: Beyond grain refinement and inclusion modification. *J. Mater. Res. Technol.* **2026**, *41*, 805–818. [CrossRef]
34. Tong, Z.P.; Zhang, Y.Z.; Wang, Y.C.; Ye, Y.X.; Yin, J.; Bao, Y.C.; Ren, X.D. Achieving strength-ductility synergy of an additively manufactured metastable high-entropy alloy via deep cryogenic treatment followed by laser shock peening. *Int. J. Extrem. Manuf.* **2026**, *8*, 015006. [CrossRef]
35. Lu, S.; Yu, Y.P.; Lai, H.C.; Zhang, Z.Y.; Chen, M.; Zheng, G.L.; Zhang, D.L. Eliminating prior chip boundaries and enhancing mechanical properties in a solid-state recycled AA6063 aluminum alloy by hot rolling. *Mater. Sci. Eng. A* **2026**, *958*, 149998. [CrossRef]

36. Sui, S.; Qi, J.W.; Ma, D.; Xu, C.J.; Qi, Y.S.; Xu, M.T.; Liu, Y.H.; Yu, W.J.; Guo, C.; Wu, X.Q.; et al. Additive manufacturing of ultrastrong and ductile nickel matrix composites via hetero-deformation induced strengthening. *Int. J. Extrem. Manuf.* **2025**, *7*, 045003. [CrossRef]
37. Zhang, X.L.; Wu, G.H.; Zhang, L.; Pang, S.; Wei, G.L.; Xie, H.; Qi, F.Z.; Sun, B.D. On the microstructural characteristics and mechanical properties of Al-2Li-2Cu-0.5 Mg alloy: The role of Yb additions. *J. Mater. Sci.* **2022**, *57*, 3688–3708. [CrossRef]
38. Chen, A.T.; Peng, Y.; Zhang, L.; Wu, G.H. Microstructural evolution and mechanical properties of cast Al-3Li-1.5Cu-0.2Zr alloy during heat treatment. *Mater. Charact.* **2016**, *114*, 234–242. [CrossRef]

Disclaimer/Publisher's Note: The statements, opinions and data contained in all publications are solely those of the individual author(s) and contributor(s) and not of MDPI and/or the editor(s). MDPI and/or the editor(s) disclaim responsibility for any injury to people or property resulting from any ideas, methods, instructions or products referred to in the content.